Glutamine-based PET imaging facilitates enhanced metabolic evaluation of gliomas *in vivo*

Sriram Venneti[1,*], **Mark P. Dunphy**[2,*], **Hanwen Zhang**[3,*], **Kenneth L. Pitter**[4], **Patrick Zanzonico**[5], **Carl Campos**[6], **Sean D. Carlin**[7], **Gaspare La Rocca**[4], **Serge Lyaschenko**[8], **Karl Ploessl**[9], **Daniel Rohle**[4,6], **Antonio M. Omuro**[10], **Justin R. Cross**[13], **Cameron W. Brennan**[5,11], **Wolfgang A. Weber**[2,3], **Eric C. Holland**[12], **Ingo K. Mellinghoff**[6,10], **Hank F. Kung**[9], **Jason S. Lewis**[3,7,8,#], and **Craig B. Thompson**[4,6,#]

[1]Department of Pathology, University of Michigan, Ann Arbor, MI, 41809

[2]Molecular Imaging & Therapy Service, Department of Radiology, MSKCC, New York, NY, 10065

[3]Molecular Pharmacology and Chemistry Program, MSKCC, New York, NY, 10065

[4]Cancer Biology and Genetics Program, MSKCC, New York, NY, 10065

[5]Medical Physics, MSKCC, New York, NY, 10065

[6]Human Oncology and Pathogenesis Program, MSKCC, New York, NY, 10065

[7]Radiochemistry & Imaging Sciences Service, Department of Radiology, MSKCC, New York, NY, 10065

[8]Radiochemistry & Molecular Imaging Probe Core, MSKCC, New York, NY, 10065

[9]Departments of Radiology and Pharmacology, University of Pennsylvania, Philadelphia, PA, 19104

[10]Department of Neurology, MSKCC, New York, NY, 10065

[11]Department of Neurosurgery, MSKCC, New York, NY, 10065

[12]Division of Human Biology, Fred Hutchinson Cancer Research Center, and Alvord Brain Tumor Center, University of Washington, Seattle, WA 98109

[13]Donald B. and Catherine C. Marron Cancer Metabolism Center, MSKCC, New York, NY, 10065

[#]Corresponding authors: Craig B. Thompson, M.D., President and CEO, Z-1245, 408 East 69th street, Memorial Sloan Kettering Cancer Center, New York, NY 10065, Phone: 212-639-6561, Fax: 212-717-3299, ThompsonC@mskcc.org. Jason S. Lewis, Ph.D., Radiochemistry & Imaging Sciences Service, Department of Radiology, Memorial Sloan Kettering Cancer Center, 1275 York Ave., New York, NY 10065. lewisj2@mskcc.org.
[*]These authors contributed equally to this study.

Competing interests

C.B.T is co-founder of Agios Pharmaceuticals and has financial interest in Agios. The other authors of this study declare that they have no competing interests.

Abstract

Glucose and glutamine are the two principal nutrients that cancer cells use to proliferate and survive. Many cancers show altered glucose metabolism, which constitutes the basis for *in vivo* positron emission tomography (PET) imaging with ^{18}F-fluorodeoxyglucose (^{18}F-FDG). However, ^{18}F-FDG is ineffective in evaluating gliomas due to high background uptake in the brain. Glutamine metabolism is also altered in many cancers, and we demonstrate that PET imaging *in vivo* with the glutamine analogue 4-[18]F-(2S,4R)-fluoroglutamine (^{18}F-FGln) shows high uptake in gliomas but low background brain uptake, facilitating clear tumor delineation. Chemo/radiation therapy reduced ^{18}F-FGln-tumor avidity, corresponding with decreased tumor burden. ^{18}F-FGln uptake was not observed in animals with a permeable blood-brain barrier or neuroinflammation. We translated these findings to human subjects, where ^{18}F-FGln showed high tumor/background ratios with minimal uptake in the surrounding brain in human glioma patients with progressive disease. These data suggest that ^{18}F-FGln is avidly taken up by gliomas, can be used to assess metabolic nutrient uptake in gliomas *in vivo,* and may serve as a valuable tool in the clinical management of gliomas.

Introduction

Cancer cells commonly undergo metabolic reprograming, enabling increased nutrient uptake and metabolism (1). Glucose and glutamine are key nutrients that cancer cells use for survival and proliferation (1, 2). Through the Warburg effect, tumors exhibit enhanced glucose uptake and metabolism by aerobic glycolysis (1, 2). This increase in glucose uptake can be evaluated *in vivo* using positron emission tomography (PET) imaging with the glucose analogue ^{18}F-fluorodeoxyglucose (^{18}F-FDG). ^{18}F-FDG PET imaging is a valuable clinical tool and is routinely used in diagnosing, grading and staging cancers and assessing the efficacy of therapies (3). However, ^{18}F-FDG is not effective in evaluating gliomas *in vivo* because the high glucose metabolism in the normal brain results in suboptimal tumor detection and delineation (4, 5). Neurologically destructive gliomas are one of the most fatal forms of cancer. Thus there is an urgent and unmet need to develop more effective clinical imaging modalities as a means to effectively and non-invasively evaluate altered nutrient uptake and metabolism in gliomas *in vivo*.

Glutamine is the other principal nutrient that tumor cells use. It is the most abundant amino acid in the plasma, and many cancers are addicted to glutamine for their survival. Cancers such as neuroblastoma, lymphoma, renal carcinoma, and pancreatic adenocarcinoma use altered glutamine metabolism to support their growth and survival. Glutamine metabolism contributes to tumor cell proliferation, ATP synthesis, and the production of biomolecules, such as proteins, lipids, and nucleic acids (6, 7). We have recently developed 4-[18]F-(2S,4R)-fluoroglutamine (^{18}F-FGln), an analogue of glutamine which is taken up by cancer cells *in vitro* and shows specific uptake on PET imaging in mouse xenograft models *in vivo* (8).

We hypothesized that glutamine addiction in gliomas can be leveraged to image gliomas *in vivo* by PET with ^{18}F-FGln to assess altered nutrient uptake in the tumors. Primary glioblastomas (GBMs) show various genetic alterations, such as platelet-derived growth factor receptor A (*PDGFRA*) amplification, phosphatase and tensin homolog (*PTEN*) loss,

and epidermal growth factor (*EGFR*) alterations (9). These molecular abnormalities converge on deregulation of the PI3K/AKT/mTOR pathway (9). Secondary GBMs and ~70% of intermediate-grade gliomas harbor mutations in isocitrate dehydrogenase 1 (IDH1), an enzyme in the TCA cycle, resulting in the production of the oncometabolite 2-hydroxyglutarate (2-HG) (10). Thus, from a metabolic perspective, gliomas fall into two broad groups: those driven by enhanced PI3K/AKT/mTOR signaling (primary GBMs) and those bearing IDH1 mutations (secondary GBMs and intermediate grade gliomas).

To address our hypothesis, we used PET imaging with ^{18}F-FGln *in vivo* to evaluate glutamine uptake in PDGF-driven glioma models with PTEN loss (to model primary GBMs with enhanced PI3K/AKT/mTOR signaling) and in IDH1-mutant (IDH1m) glioma models. The data demonstrate that ^{18}F-FGln showed high uptake in both glioma models but minimal uptake in the normal brain, enabling clear tumor visualization. Further, ^{18}F-FGln specifically delineated gliomas *in vivo* by PET imaging in animal models and in human glioma patients with disease progression. The results suggest that ^{18}F-FGln may serve as a valuable clinical tool in the assessment of metabolic nutrient uptake in gliomas *in vivo* using PET imaging.

Results

^{18}F-FGln shows high uptake in gliomas but negligible uptake in the normal brain

Because glutamine is an important source of replenishment of TCA cycle metabolites (termed anaplerosis) in many cancers, we first evaluated the contribution of glutamine to TCA cycle anaplerosis in glioma cell lines bearing various oncogenes: U87-MG (PTEN −/−), TS543 (PDGFRA, PTEN −/−), and TS603 (IDH1m). Glutamine was the main TCA cycle anaplerotic substrate in all cell lines tested (Figure S1), underscoring the importance of glutamine as a key nutrient in gliomas and the rationale for developing glutamine-based PET imaging of gliomas. To determine if fluorinated glutamine is metabolized to glutamate, we compared ^{19}F-FGln (identical to ^{18}F-FGln, except that ^{18}F is replaced with the more stable fluorine isotope ^{19}F to enable GC-mass spectroscopy analyses) with [U-^{13}C]-glutamine metabolism in the above cell lines. Whereas [U-^{13}C]-glutamine was metabolized to [U-^{13}C]-glutamate, no ^{19}F-glutamate was detected (in comparison to standards) suggesting that ^{19}F-FGln is not converted to ^{19}F-glutamate (Figure S2). These *in vitro* data with ^{19}F-FGln are similar to ^{18}F-FGln data *in vivo,* where a only minor fraction of ^{18}F-FGln (~9% in animal tumor xenografts (*8*)) is converted to ^{18}F-glutamate, suggesting that ^{18}F-FGln PET imaging is mainly a measure of glutamine uptake.

To assess glutamine uptake *in vivo* in gliomas we used PET imaging with the glutamine analogue ^{18}F-FGln (Figure 1A). Biodistribution studies with ^{18}F-FGln in normal mice (Figure S3) showed that ^{18}F-FGln crossed the blood-brain barrier (BBB) but showed minimal uptake in the normal brain compared to other organs such as the pancreas and the gut (Figures 1 and S3). We thus postulated that high glutamine utilization in gliomas (Figure S1) coupled with minimal uptake in the normal brain (Figures 1 and S3) would result in high tumor-to-background ratios. To test this, we compared ^{18}F-FGln and ^{18}F-FDG uptake in the normal mouse brain with glioma xenografts. Xenograft models were created by subcutaneously injecting TS543 (*PDGFRA*, *PTEN* −/−), TS603 (IDH1m), TS598 (*EGFR*),

and U87-MG (*PTEN* −/−) glioma cells into SCID mice. Xenografts histopathologically resembled human gliomas (9) (Figure S4A–D). Fasting or perfusion did not have any effect on ^{18}F-FGln uptake in glioma subcutaneous xenografts (Figure S5). Further, ^{18}F-FGln uptake was significantly (p=0.0088) lowered in xenografts on co-injection of excess cold ^{19}F-FGln (Figure S3). All glioma subcutaneous xenografts showed significantly (p<0.0001) higher uptake of ^{18}F-FGln compared to the normal brain (Figure 1 and Figure S6, whole body images). ^{18}F-FDG showed higher or equivalent uptake in the normal brain compared to all tested glioma subcutaneous xenografts (Figure 1 and Figure S6, whole body images).

In IDH1-mutant glioma cells, we found that [U-^{13}C]-glutamine was metabolized to generate the oncometabolite 2-hydroxyglutarate. This was reversed by either shRNA knockdown of total *IDH1* (mutant and wild type) or an IDH1m-specific inhibitor (IDH35) (11) *in vitro* (Figures S1 I and S7). Glioma xenografts bearing shRNA against total IDH1 did not show significant alterations in ^{18}F-FGln uptake compared to controls (Figure S7). This suggests that ^{18}F-FGln uptake *in vivo* in TS603 IDH1m cells is not altered when the activity of mutant IDH1 generating 2-HG is inhibited (Figure S7).

^{18}F-FGln enables distinct delineation of gliomas *in vivo*

We next evaluated well-characterized genetically engineered glioma mouse models using the RCAS/tv-a system driven by PDGF with a PTEN-null background (RCAS-PDGF, *PTEN* −/−), which develop GBM histologically identical to human GBM (Figure S4E and G) (12). PET imaging in these animals showed marked ^{18}F-FGln uptake with distinct tumor delineation (compared to the surrounding brain) in a region directly corresponding to the tumor, as detected by MRI and confirmed by autoradiography and histopathology (Figure 2A–F). Tumor-to-background ratios with ^{18}F-FGln ranged from 4:1 to 6:1 compared to ~1:1 tumor-to-background ratio with ^{18}F-FDG (Figure 2F). Similar findings were observed in RCAS-PDGF animals on a PTEN wild type background (Figure S8A–D) and in an orthotopic IDH1m glioma model (Figure 2G–L and S8 E–G).

^{18}F-FGln uptake is not observed in neuroinflammation or BBB disruption

To evaluate if inflammatory cells contributed to ^{18}F-FGln uptake, we created mouse models of neuroinflammation (Figure 3A). Lipopolysaccharide (LPS) injection into the brain resulted in global activation of IBA1 immunoreactive microglia/macrophages in the injected hemisphere well beyond the injection site (Figures 3B and S9A–D). We also used IFN-γ which polarizes macrophages/microglia towards classic activation, and IL-4, which mediates an alternative activation phenotype similar to tumor-associated macrophages (13). Robust neuroinflammation was confirmed histopathologically (Figure 3B and Figure S9A–D). Mice were imaged at the peak of neuroinflammation with ^{18}F-FGln and ^{18}F-FDG (Figures 3C–E and S9E–G). ^{18}F-FDG PET is generally a poor measure of neuroinflammation in mouse brains *in vivo* because of the high background uptake in the brain (14). Consistent with this, no lesion was discernible with ^{18}F-FDG PET (Figure 3D and S9F). Conversely, ^{18}F-FGln did not show any uptake at the site of the lesion in neuroinflammatory models, as opposed to the high uptake seen in gliomas (Figure 3C and Figure S9E).

To address the concern of BBB permeability as a factor in causing increased ^{18}F-FGln delivery to the brain, we used an adenosine receptor agonist that is an established means of increasing BBB permeability by increasing spaces between endothelial cells in brain capillaries (15, 16). NECA [1-(6-amino-9H-purin-9-yl)-1-deoxy-N-ethyl-β-D-ribofuranuronamide], a combined A1 and A2 adenosine receptor agonist, significantly (p=0.034) increased BBB permeability in mice as determined by measuring extravasation of fluorescent-labeled dextran into the brain (Figure 3F and G). We did not see increased ^{18}F-FGln delivery to the brain in NECA–treated animals (Fig 3H–K), suggesting that increased BBB permeability by itself does not artificially increase ^{18}F-FGln delivery to the brain. This demonstrates that neuroinflammation or a breach in the BBB using NECA do not significantly contribute to ^{18}F-FGln uptake.

^{18}F-FGln uptake in gliomas is reduced after chemo/radiation therapy

To evaluate if ^{18}F-FGln can monitor treatment efficacy and differentiate tumor from post-treatment changes, we studied a well-characterized RCAS-PDGF-PTEN null mouse model of radiation/chemotherapy (17) (Figures 4A and S10A–C). The same mouse was imaged before therapy and after treatment with MRI, ^{18}F-FGln, and ^{18}F-FDG (Figure 4B–F). As can be seen in post-treatment changes in human patients, the T2-weighted MRI showed no appreciable differences when comparing before-treatment scans with after-treatment scans (18). In contrast, ^{18}F-FGln showed a significant reduction (p=0.0078) in tumor uptake after treatment, which was confirmed by autoradiography (Figure 4C–F).

To assess the mechanism by which chemo/radiation therapy results in a decrease in ^{18}F-FGln uptake, we compared before-treatment and after-treatment glioma brain tissues. Tumor burden was dramatically reduced after treatment, as demonstrated by a reduction in the Olig2-positive tumor cells (p=0.031) (Figure S10A–B). Brain tissues after treatment showed increased reactive gliosis in the form of GFAP-positive astrocytosis and abundant IBA1-positive macrophages/microglia (Figure S11A–B). No significant changes were noted in CD3-positive lymphocyte infiltration or in blood vessels as delineated by CD31 staining for endothelial cells and collagen staining for vessel walls (Figure S11C–E). Moreover, expression of the glutamine transporter SLC1A5 in residual tumor cells after treatment was not significantly different from that seen in tumor cells before treatment (Figure S11F). These data suggest that reduction in ^{18}F-FGln uptake after chemo/radiation therapy is due a decrease in tumor burden. Further, these data imply that ^{18}F-FGln is taken up specifically in tumor cells, can monitor treatment responses, and potentially differentiate post-treatment changes from tumor in glioma animal models.

^{18}F-FGln shows high tumor to brain uptake ratio in human gliomas with progression

To determine if our findings could be translated to a spectrum of human gliomas apart from the animal models studied, we evaluated the expression of the glutamine transporter SLC1A5, which in part mediates ^{18}F-FGln uptake (8, 19), as demonstrated by siRNA knockdown and pharmacologic inhibition (Figure S12A–B). Immunohistochemistry in normal brain tissue samples (n=8, Figure S12C) showed minimal expression, mirroring low background ^{18}F-FGln uptake. In contrast, SLC1A5 demonstrated higher expression in various gliomas (n=64), consistent with high ^{18}F-FGln-glioma uptake (Figure S12 C–D).

Further, we queried the GBM cancer genome atlas for *SLC1A5* mRNA expression, which was noted in all GBM subtypes (Figure S12E). These data suggest that ^{18}F-FGln uptake is not restricted to the animal model glioma genotypes tested and may be of broader utility in evaluating uptake of glutamine as a key nutrient in gliomas.

We translated these findings *in vivo* to human glioma subjects as an initial investigation of ^{18}F-FGln PET imaging in human cancer patients (Phase I study, Figures 5A–L, S13, S14 A–C and S15 A–C). As part of this study, we compared ^{18}F-FGln uptake in 3 glioma patients with clinical progression of disease and 3 patients with stable disease (Tables S1 and S2). Normal brain parenchyma showed minimal ^{18}F-FGln uptake, and ^{18}F-FGln-avidity was noted in all tumors that showed progression within the 3 patients (tumor:brain ratio range: 3.7–4.8, Figures 5L and S14 and Tables S2–S3). In contrast, clinically stable tumors showed minimal or no ^{18}F-FGln-avidity on PET (Figure S15 and Table S2). Normal brain tissues in these same patients demonstrated high ^{18}F-FDG avidity, with normal brain ^{18}F-FDG concentrations (SUV) equivalent to or greater than tumor SUV values (tumor:brain ratio range: 0.9–1.0, Figure 5L and Table S2). For example, in patient #5, ^{18}F-FDG could distinguish the posterior portion of the tumor (Figure 5C, 3 red arrows) from the surrounding brain, but not the anterior part (2 red arrows, Figure 5C). In contrast, both regions of the tumor showed high uptake with ^{18}F-FGln (Figure 5B & E). This is an important issue considering the infiltrative nature of gliomas. Further, this patient's tumor demonstrated mild contrast enhancement on gadolinium-enhanced MRI (Figure 5A), but high ^{18}F-FGln avidity (Figures 5B and E) and retention of ^{18}F-FGln compared to its rapid clearance in the blood (Figure 5F). Whole body PET images, plasma and blood time activity curves, biodistribution, tracer metabolite analysis, and dosimetry from these glioma patients are provided in the supplementary information (Figures S14–S16 and Table S3–5) These findings in human subjects recapitulate our ^{18}F-FGln PET and ^{18}F-FDG PET findings in mouse models and demonstrate that clinical ^{18}F-FGln PET can evaluate high-grade glioma *in vivo* and may be potentially useful in identifying tumors undergoing transformation.

Discussion

The two principal nutrients that cancers depend on are glucose and glutamine, and metabolism of these nutrients via glycolysis and glutaminolysis is vital for cancer survival and growth (1, 2). We aimed specifically to develop a means of non-invasively assessing nutrient uptake in gliomas. ^{18}F-FDG as a measure for metabolic glucose uptake is ineffective in gliomas because of the high background in the surrounding brain. To begin to address this gap in our knowledge, we examined whether glutamine addiction displayed by many cancer cells can be leveraged to detect glutamine uptake in gliomas *in vivo* using ^{18}F-FGln. Building on our initial characterization of ^{18}F-FGln (8), in the current study we: (1) demonstrate that gliomas, due to their glutamine addiction, show high uptake of ^{18}F-FGln and that the normal brain shows minimal uptake, enabling clear tumor distinction, (2) report the use of ^{18}F-FGln in human patients, and (3) show that ^{18}F-FGln could monitor treatment response in preclinical glioma models. We do not propose that glutamine is superior to current imaging standards, but that glutamine-based PET imaging enables assessment of metabolic nutrient uptake, providing complementary information about the metabolic status of gliomas.

High tumor avidity of ^{18}F-FGln with minimal uptake in the surrounding brain enabled clear tumor delineation in all glioma animal models tested. No ^{18}F-FGln uptake was noted in a model of impaired BBB or multiple animal models of neuroinflammation. ^{18}F-FGln uptake is mainly mediated by the amino acid transporter SLC1A5 (8, 19), which was minimally expressed in the normal brain but markedly increased in gliomas. GC-mass spectroscopy analysis showed that FGln was not metabolized to F-glutamate. Further, we have previously shown that 60–70% of ^{18}F-FGln is incorporated into protein (8, 19), and we now suggest a model wherein ^{18}F-FGln is taken up mainly by SLC1A5 and is trapped in glioma cells by incorporation into proteins.

As part of our human trial of ^{18}F-FGln for clinical PET imaging, high ^{18}F-FGln avidity was noted in gliomas with progression in contrast to low background brain uptake. Additionally, no relationship was observed between contrast enhancement and ^{18}F-FGln avidity. For example, patient #5 with mild contrast enhancement demonstrated the highest ^{18}F-FGln avidity and retention of ^{18}F-FGln compared to rapid clearance in the blood. If the tumor activity on PET were merely due to BBB breakdown, the data plot would instead demonstrate progressive clearance of tracer from the tumor region, in parallel with tracer clearance from the blood pool. Although we cannot rule out effects of BBB alteration entirely, human and animal data together suggest that the relatively high ^{18}F-FGln avidity of in gliomas is not solely a function of tumor BBB disruption.

A limitation of this study is that the isotope shows bone uptake in animal models and humans (including axial uptake), with free fluorine-18 detected in the blood of all patients, implying that *in vivo* defluorination occurs. Peripheral bony uptake was minimal compared to axial uptake, suggesting uptake by bone marrow cells. To evaluate the impact of free fluoride on organ uptake of ^{18}F-FGln, we compared the biodistribution of ^{18}F-sodium fluoride as a control with that of ^{18}F-FGln. ^{18}F-sodium fluoride showed high bony uptake, but free fluoride uptake within various organs, including the brain was minimal. In contrast, ^{18}F-FGln showed lower bony uptake, but higher uptake in all organs compared to ^{18}F-sodium fluoride. These data suggest that free fluoride does not majorly contribute to specific uptake of ^{18}F-FGln within various organs. Moreover, tracer uptake in the skull did not obscure glioma ^{18}F-FGln PET evaluations, because gliomas are restricted to the brain and do not invade the skull or metastasize to bone. Another limitation is the small sample size of the glioma subjects assessed. However, despite this small sample size, data from human subjects closely mirror data from glioma cell lines and animal models, as evidenced by high ^{18}F-FGln glioma uptake and low avidity in the surrounding brain. Further, one of the prerequisites of the FDA-approved, human microdose, open label, Phase I trial was for every patient to have a tissue diagnosis prior to imaging. This precluded imaging any surgery-naive patients. Despite these limitations, the data presented support an exploratory proof-of-principle concept that ^{18}F-FGln could be potentially used as an imaging agent in glioma patients.

Non-invasive imaging forms an integral part of the clinical management of glioma patients. T1-weighted MRI with or without gadolinium is the current neuroimaging standard in glioma assessment (20). MRI provides vital anatomic and structural information and is helpful in characterizing tumors using FLAIR and in assessing BBB disruption using

gadolinium contrast enhancement, but it does not provide information on nutrient uptake and metabolism. Newer modalities such as MR spectroscopy or perfusion/diffusion-weighted MRI are beginning to address these limitations (21, 22). PET imaging agents such as [^{11}C]methionine (MET), [^{18}F]fluorothymidine (FLT), [^{18}F]-DOPA, and [^{18}F]fluoroethyl-l-tyrosine (FET) have also been used to image gliomas (23, 24). We do not propose that ^{18}F-FGln is superior to many of these current neuroimaging modalities, but that ^{18}F-FGln may provide complementary biological information specifically about metabolic nutrient uptake relevant to glioma pathology. More recently, ^{18}F-labeled glutamate (4*S*)-4-(3-^{18}F-fluoropropyl)-l-glutamate (Bayer ligand BAY 94-9392/^{18}F-FSPG) as a PET tracer has been described in preclinical models and human subjects (25, 26). This tracer relies on the x(C) (−) cysteine/glutamate exchanger system and is thought to label intracellular glutamate pools (25). Our goal is to translate a specific nutrient metabolic pathway that is biologically relevant to the pathology of gliomas to a clinically useful imaging modality. Indeed, ^{18}F-FGln PET imaging takes advantage of glutamine addiction in gliomas and may serve as a valuable tool to assess metabolic glutamine uptake in gliomas *in vivo*. Low uptake in the normal brain may also help in evaluating CNS metastasis.

Mice treated with chemo/radiation therapy showed a profound reduction in ^{18}F-FGln uptake after treatment, corresponding to a decrease in tumor volume. Brain vasculature (CD34-positive and collagen IV-positive blood vessel walls) did not differ before and after treatment. Although these data suggest that vasculature may not be altered in this model, we cannot entirely rule out other changes in the vasculature or the BBB that may contribute to reduced ^{18}F-FGln uptake after treatment. However, neuroinflammatory models showed no ^{18}F-FGln uptake and taken together with reduced uptake after treatment, suggest that ^{18}F-FGln may be potentially useful in differentiating non-neoplastic, post-treatment and inflammatory changes from tumor. Data from our small sample size of patients suggest that ^{18}F-FGln may also be useful in monitoring progression of gliomas as they transform to more metabolically active and aggressive tumors. In summary, the studies suggest that glutamine-based PET imaging with ^{18}F-FGln may be an important measure of glutamine uptake in gliomas *in vivo* and may serve as a valuable tool in the clinical management of gliomas.

Materials and methods

Study Design

The objective of this study was to address the clinically unmet need of assessing metabolic nutrient uptake in gliomas *in vivo*. This goal was addressed by (1) evaluating glutamine uptake in gliomas by PET imaging in clinically relevant glioma animal models, (2) assessing if glutamine PET-based imaging could monitor therapeutic response in glioma animal models, and (3) translating these findings to human subjects.

All animal experiments were performed after approval from the MSKCC Institutional Animal Care and Use Committee and were conducted as per NIH guidelines for animal welfare. The utility of glutamine-based PET imaging to monitor therapeutic response was assessed using standard chemo/radiation therapy protocols in glioma animal models. Animals were randomly assigned to various test groups in a blinded manner. Individuals

handling the animals and conducting animal surgeries and therapies were blinded to the experimental design. Evaluation of ^{18}F-FGln PET uptake measurements in animals was performed in a non-blinded fashion. Because ^{18}F-FGln microPET imaging is a new imaging technology, it is difficult to estimate sample size with adequate power. An n = 3 – 9 was selected for these well-controlled models with a low (<10%) error in consecutive studies. Cell culture studies were conducted using three independent experiments (27). No samples or animals were excluded from data analyses.

Human glioma subjects were studied as part of an in-human microdose, open label, Phase I trial of ^{18}F-FGln PET that was approved by the institutional review board and conducted under the auspices of an FDA-approved investigational new drug application in compliance with the STAndards for the Reporting of Diagnostic accuracy studies (STARD) guidelines for diagnostic studies (trial registered at www.clinicaltrial.gov; NCT01697930). Informed consent was obtained before imaging.

Animal models of gliomas

Subcutaneous glioma xenografts were created by inoculating SCID mice (4–6 weeks of age, male and female, NOD-SCID, Taconic Farms Inc.) with 1×10^6 U87-MG, TS603, TS543, or TS598 cells resuspended in 200 µL of a 1:1 volume of cell culture medium and matrigel (BD Biosciences). Animals were imaged when xenograft tumor volumes approached 200 mm^3. Genetically modified glioma models were generated using the RCAS/tva system. 4–6 week-old, male or female C57BL6 *Nestin*-tv-a/*Ink4a-Arf*–/– mice with or without a PTEN fl/fl background were anesthetized with ketamine (0.1 mg/g) and xylazine (0.02 mg/g) and injected using a stereotactic fixation device (Stoelting) (17). One µL of RCAS-PDGF or a 1:1 mixture of 4×10^4 RCAS-PDGF and RCAS-Cre transfected DF1 cells were delivered using a 30-gauge needle attached to a Hamilton syringe. Cells were injected into the right frontal cortex (stereotactic coordinates: bregma +1.7 mm (anterior), lateral −0.5 mm (right), and at a depth of 2.5 mm). For orthotopic injection of glioma cells, the same procedure was followed, except that TS603 IDH1m (1×10^6 cells) was implanted into the right frontal cortex (same coordinates as above). Individuals performing implantation and stereotactic injections were blinded to the experimental design.

Small animal PET imaging

Animals were imaged with ^{18}F-FDG and ^{18}F-FGln (24 hours apart to allow complete decay of radiotracer) by injecting 200 µCi of the radiotracer into the lateral tail vein. PET imaging was performed using a dedicated small-animal microPET scanner (Concorde Microsystems) under 2% isoflurane anesthesia, with the tumors centered in the field of view. Dynamic imaging was performed by obtaining sixty-minute acquisitions with an energy window of 350–750 keV with a coincidence-timing window of 6 ns. For static imaging, acquisitions were collected 0.5 h, 1 h and 2 h after injection. In each animal, the MRI and PET images were directly compared. Region-of-interest (ROI) analysis of the acquired images was performed using ASIPro software (Siemens) in a non-blinded manner, and the observed maximum pixel value was represented as percent-injected dose/cubic centimeter (%ID/cc).

Tumor to brain ratios were determined by normalizing tumor uptake to surrounding brain uptake.

^{18}F-FGln synthesis

Synthesis of the precursor for ^{18}F-(2S,4R)4F-Gln (^{18}F-FGln) was performed as described(8, 28). Briefly, the radiolabeling procedure was similar except that the radiolabeling was performed at 90°C, and the final compound (in saline) was passed through a C^{18} cartridge and AG11A8 resin to formulate the final solution for injection. The purity of ^{18}F-FGln was analyzed with a chiral column (Chirex 3126 (d)-penicillamine, 1 mM $CuSO_4$ solution, 1 mL/min). For human subjects, ^{18}F-FGln was manufactured at the MSKCC Radiochemistry and Molecular Probe Core Facility pursuant to an Investigational New Drug Application (IND) acknowledged by the United States Food and Drug Administration (US FDA). Every batch of final drug product was tested to assure conformance to the drug product acceptance specifications, which included radiochemical purity (≥80%) and identity, residual solvent content, endotoxin content, radionuclidic identity, pH, and appearance. 125 MBq was adequate for imaging the brain region-of-interest and provided satisfactory PET image quality and count statistics.

^{18}F-FGln PET-CT protocol

Microdose ^{18}F-FGln tracer was administered to patients by single peripheral intravenous injection of 125 MBq as a slow bolus (1 minute duration) in a volume of 5–10 mL. Imaging of ^{18}F-FGln biodistribution was obtained at approximately 30, 90, and 160 min after injection, using a Discovery DSTE PET-CT scanner (GE Healthcare) with the patient supine upon the scanner bed. After a scout X-ray, CT data were acquired with 140 kvp; 70 mA; pitch of 1.75:1; reconstructed slice thickness of 3.75 mm; 0.8 s per rotation. CT data were reconstructed in a 512 × 512 matrix using a filtered back-projection algorithm. PET emission scans were acquired starting at the proximal thigh region and ending at the head region; emission scanning specifically of the brain tumor field of view shown was acquired as a single bed position of 35 minutes duration in 3–D mode. PET images were reconstructed using an ordered subset expectation maximization iterative algorithm. PET/CT scans obtained at the 60 and 150 minutes post-injection time-points also spanned thighs to skull using the same X-ray/CT and PET emission data acquisitions and reconstructions. PET emission data were reconstructed using an ordered subset expectation maximization iterative algorithm. Emission data were corrected for random detector inhomogeneity, scatter, attenuation, deadtime, and decay. PET, CT, and fusion PET-CT images shown were generated for display using an integrated GE PACS AW Suite workstation (GE Healthcare). PET data was analyzed using HERMES workstation (Hermes Medical Solutions).

Statistical analysis

Statistical analyses were performed in consultation with the Sloan Kettering biostatistics facility. Data are represented as the means ± standard errors (s.e.m.) unless specified otherwise. Graphs were plotted and statistical analyses were performed using Prism software (version 6, Graphpad). All statistical tests were two-sided. Unpaired, two-tailed, Student's *t* test or one-way ANOVA followed by post hoc Bonferroni, Dunnett's, or Tukey's multiple

comparisons analysis were used to analyze data. Wilcoxon matched-pairs signed rank *t* test was used when the same parameter was assessed in the same animal in any given experiment (chemo/radiation therapy when the same animal was imaged with a given radioligand before and after treatment). Data were considered significant if *p* values were below 0.05 (95% confidence intervals).

Supplementary Material

Refer to Web version on PubMed Central for supplementary material.

Acknowledgments

References and Notes

1. Ward PS, Thompson CB. Metabolic reprogramming: a cancer hallmark even warburg did not anticipate. Cancer Cell. 2012; 21:297–308. [PubMed: 22439925]

2. Vander Heiden MG, Cantley LC, Thompson CB. Understanding the Warburg effect: the metabolic requirements of cell proliferation. Science. 2009; 324:1029–1033. [PubMed: 19460998]

3. Weber WA, Schwaiger M, Avril N. Quantitative assessment of tumor metabolism using FDG-PET imaging. Nuclear medicine and biology. 2000; 27:683–687. [PubMed: 11091112]

4. Klasner BD, Krause BJ, Beer AJ, Drzezga A. PET imaging of gliomas using novel tracers: a sleeping beauty waiting to be kissed. Expert review of anticancer therapy. 2010; 10:609–613. [PubMed: 20469990]

5. Petrirena GJ, Goldman S, Delattre JY. Advances in PET imaging of brain tumors: a referring physician's perspective. Curr Opin Oncol. 2011; 23:617–623. [PubMed: 21825989]

6. DeBerardinis RJ, Mancuso A, Daikhin E, Nissim I, Yudkoff M, Wehrli S, Thompson CB. Beyond aerobic glycolysis: transformed cells can engage in glutamine metabolism that exceeds the requirement for protein and nucleotide synthesis. Proc Natl Acad Sci U S A. 2007; 104:19345–19350. [PubMed: 18032601]

7. Wise DR, Thompson CB. Glutamine addiction: a new therapeutic target in cancer. Trends Biochem Sci. 2010; 35:427–433. [PubMed: 20570523]

8. Lieberman BP, Ploessl K, Wang L, Qu W, Zha Z, Wise DR, Chodosh LA, Belka G, Thompson CB, Kung HF. PET of Glutaminolysis in Tumors by 18F-(2S,4R)4-Fluoroglutamine. J Nucl Med. 2011

9. Huse JT, Holland EC. Targeting brain cancer: advances in the molecular pathology of malignant glioma and medulloblastoma. Nat Rev Cancer. 2010; 10:319–331. [PubMed: 20414201]

10. Dang L, White DW, Gross S, Bennett BD, Bittinger MA, Driggers EM, Fantin VR, Jang HG, Jin S, Keenan MC, Marks KM, Prins RM, Ward PS, Yen KE, Liau LM, Rabinowitz JD, Cantley LC,

Thompson CB, Vander Heiden MG, Su SM. Cancer-associated IDH1 mutations produce 2-hydroxyglutarate. Nature. 2010; 465:966. [PubMed: 20559394]

11. Rohle D, Popovici-Muller J, Palaskas N, Turcan S, Grommes C, Campos C, Tsoi J, Clark O, Oldrini B, Komisopoulou E, Kunii K, Pedraza A, Schalm S, Silverman L, Miller A, Wang F, Yang H, Chen Y, Kernytsky A, Rosenblum MK, Liu W, Biller SA, Su SM, Brennan CW, Chan TA, Graeber TG, Yen KE, Mellinghoff IK. An inhibitor of mutant IDH1 delays growth and promotes differentiation of glioma cells. Science. 2013; 340:626–630. [PubMed: 23558169]

12. Hambardzumyan D, Amankulor NM, Helmy KY, Becher OJ, Holland EC. Modeling Adult Gliomas Using RCAS/t-va Technology. Transl Oncol. 2009; 2:89–U45. [PubMed: 19412424]

13. Mills CD. M1 and M2 Macrophages: Oracles of Health and Disease. Critical reviews in immunology. 2012; 32:463–488. [PubMed: 23428224]

14. Wu C, Li F, Niu G, Chen X. PET imaging of inflammation biomarkers. Theranostics. 2013; 3:448–466. [PubMed: 23843893]

15. Carman AJ, Mills JH, Krenz A, Kim DG, Bynoe MS. Adenosine receptor signaling modulates permeability of the blood-brain barrier. J Neurosci. 2011; 31:13272–13280. [PubMed: 21917810]

16. Gao X, Qian J, Zheng S, Changyi Y, Zhang J, Ju S, Zhu J, Li C. Overcoming the blood-brain barrier for delivering drugs into the brain by using adenosine receptor nanoagonist. ACS nano. 2014; 8:3678–3689. [PubMed: 24673594]

17. Leder K, Pitter K, Laplant Q, Hambardzumyan D, Ross BD, Chan TA, Holland EC, Michor F. Mathematical Modeling of PDGF-Driven Glioblastoma Reveals Optimized Radiation Dosing Schedules. Cell. 2014; 156:603–616. [PubMed: 24485463]

18. Tran DK, Jensen RL. Treatment-related brain tumor imaging changes: So-called "pseudoprogression" vs. tumor progression: Review and future research opportunities. Surgical neurology international. 2013; 4:S129–135. [PubMed: 23682339]

19. Ploessl K, Wang LM, Lieberman BP, Qu WC, Kung HF. Comparative Evaluation of F-18-Labeled Glutamic Acid and Glutamine as Tumor Metabolic Imaging Agents. Journal of Nuclear Medicine. 2012; 53:1616–1624. [PubMed: 22935578]

20. Dhermain FG, Hau P, Lanfermann H, Jacobs AH, van den Bent MJ. Advanced MRI and PET imaging for assessment of treatment response in patients with gliomas. Lancet neurology. 2010; 9:906–920.

21. Shiroishi MS, Booker MT, Agarwal M, Jain N, Naghi I, Lerner A, Law M. Posttreatment evaluation of central nervous system gliomas. Magnetic resonance imaging clinics of North America. 2013; 21:241–268. [PubMed: 23642552]

22. Brandao LA, Shiroishi MS, Law M. Brain tumors: a multimodality approach with diffusion-weighted imaging, diffusion tensor imaging, magnetic resonance spectroscopy, dynamic susceptibility contrast and dynamic contrast-enhanced magnetic resonance imaging. Magnetic resonance imaging clinics of North America. 2013; 21:199–239. [PubMed: 23642551]

23. la Fougere C, Suchorska B, Bartenstein P, Kreth FW, Tonn JC. Molecular imaging of gliomas with PET: opportunities and limitations. Neuro Oncol. 2011; 13:806–819. [PubMed: 21757446]

24. Crippa F, Alessi A, Serafini GL. PET with radiolabeled aminoacid. Q J Nucl Med Mol Imaging. 2012; 56:151–162. [PubMed: 22617237]

25. Koglin N, Mueller A, Berndt M, Schmitt-Willich H, Toschi L, Stephens AW, Gekeler V, Friebe M, Dinkelborg LM. Specific PET imaging of xC- transporter activity using a (1)(8)F-labeled glutamate derivative reveals a dominant pathway in tumor metabolism. Clin Cancer Res. 2011; 17:6000–6011. [PubMed: 21750203]

26. Baek S, Mueller A, Lim YS, Lee HC, Lee YJ, Gong G, Kim JS, Ryu JS, Oh SJ, Lee SJ, Bacher-Stier C, Fels L, Koglin N, Schatz CA, Dinkelborg LM, Moon DH. (4S)-4-(3-18F-fluoropropyl)-L-glutamate for imaging of xC transporter activity in hepatocellular carcinoma using PET: preclinical and exploratory clinical studies. J Nucl Med. 2013; 54:117–123. [PubMed: 23232273]

27. Wise DR, Ward PS, Shay JE, Cross JR, Gruber JJ, Sachdeva UM, Platt JM, Dematteo RG, Simon MC, Thompson CB. Hypoxia promotes isocitrate dehydrogenase-dependent carboxylation of alpha-ketoglutarate to citrate to support cell growth and viability. Proc Natl Acad Sci U S A. 2011

28. Qu WC, Zha ZH, Ploessl K, Lieberman BP, Zhu L, Wise DR, Thompson CB, Kung HF. Synthesis of Optically Pure 4-Fluoro-Glutamines as Potential Metabolic Imaging Agents for Tumors. J Am Chem Soc. 2011; 133:1122–1133. [PubMed: 21190335]

29. Venneti S, Lopresti BJ, Wang G, Slagel SL, Mason NS, Mathis CA, Fischer ML, Larsen NJ, Mortimer AD, Hastings TG, Smith AD, Zigmond MJ, Suhara T, Higuchi M, Wiley CA. A comparison of the high-affinity peripheral benzodiazepine receptor ligands DAA1106 and (R)-PK11195 in rat models of neuroinflammation: implications for PET imaging of microglial activation. J Neurochem. 2007; 102:2118–2131. [PubMed: 17555551]

30. Phillips E, Penate-Medina O, Zanzonico PB, Carvajal RD, Mohan P, Ye Y, Humm J, Gonen M, Kalaigian H, Schoder H, Strauss HW, Larson SM, Wiesner U, Bradbury MS. Clinical translation of an ultrasmall inorganic optical-PET imaging nanoparticle probe. Science translational medicine. 2014; 6:260ra149.
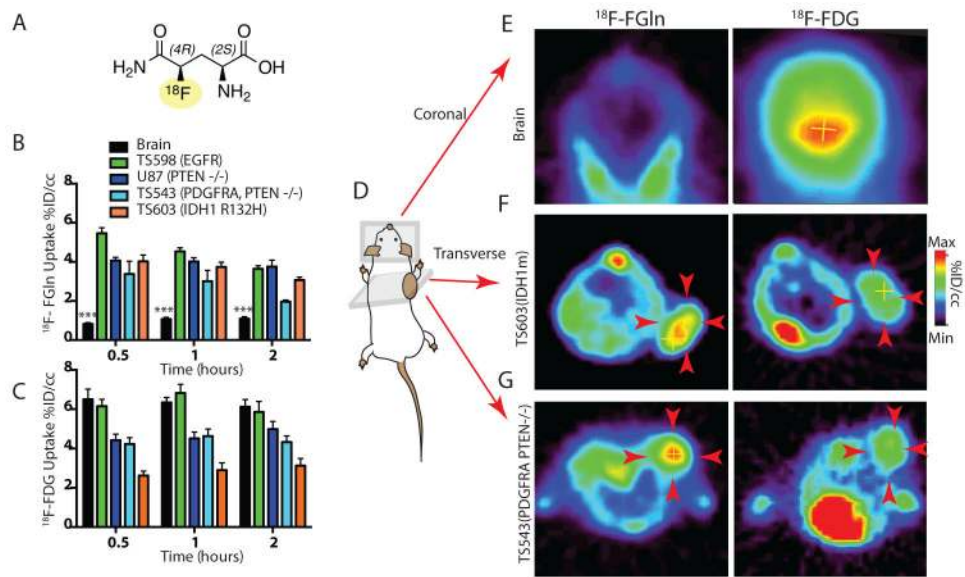
Fig 1. ^{18}F-FGln shows high uptake in glioma xenografts and low background in normal brain
A. Illustration of the structure of ^{18}F-FGln.

B. Comparison of ^{18}F-FGln uptake at 0.5, 1, and 2 hours after injection in the normal brain (black bars, n=6 for all time points) with glioma xenografts: TS598 with EGFR amplification (green bars, n=6 for all time points), U-87 MG with PTEN deletion (dark blue bars, n=5 for all time points), TS543 with PDGFRA amplification and PTEN deletion (light blue bars, n=5 for 0.5 and 1 h time points, n=4 for 2 h time point), and TS603 with IDH1 R132H mutations (orange bars, n=5 for all time points). %ID/cc: percent injected dose/cubic centimeter. Statistical significance was determined by two-sided ANOVA; *** indicates p < 0.001.

C. Comparison of ^{18}F-FDG uptake at 0.5, 1, and 2 hours after injection in the normal brain (black bars, n=6 for all time points) with glioma xenografts: TS598 with EGFR amplification (green bars, n=3 for 0.5 and 1 h and n=6 for 2 h), U-87 MG with PTEN deletion (dark blue bars, n=5 for all time points), TS543 with PDGFRA amplification and PTEN deletion (light blue bars, n=6 for 0.5 h and n=4 for 1 h and 2 h time points), and TS603 with IDH1 R132H mutations (orange bars, n=5 for all time points) %ID/cc: percent injected dose/cubic centimeter.

D. Illustration of mouse with glioma xenograft implanted in the shoulder region, indicating coronal and transverse planes along which PET images were captured.

E. Representative coronal PET images of the normal skull and brain depicting ^{18}F-FGln and ^{18}F-FDG uptake.

F. Representative transverse PET images (see figure S5 for full body coronal images) showing ^{18}F-FGln and ^{18}F-FDG uptake in TS603 (IDH1 R132H) glioma xenografts (indicated by red arrows).

G. Representative transverse PET images (see figure S5 for full body coronal images) showing ^{18}F-FGln and ^{18}F-FDG uptake in TS543 (PDGFRA, PTEN −/−) glioma xenografts (indicated by red arrows).
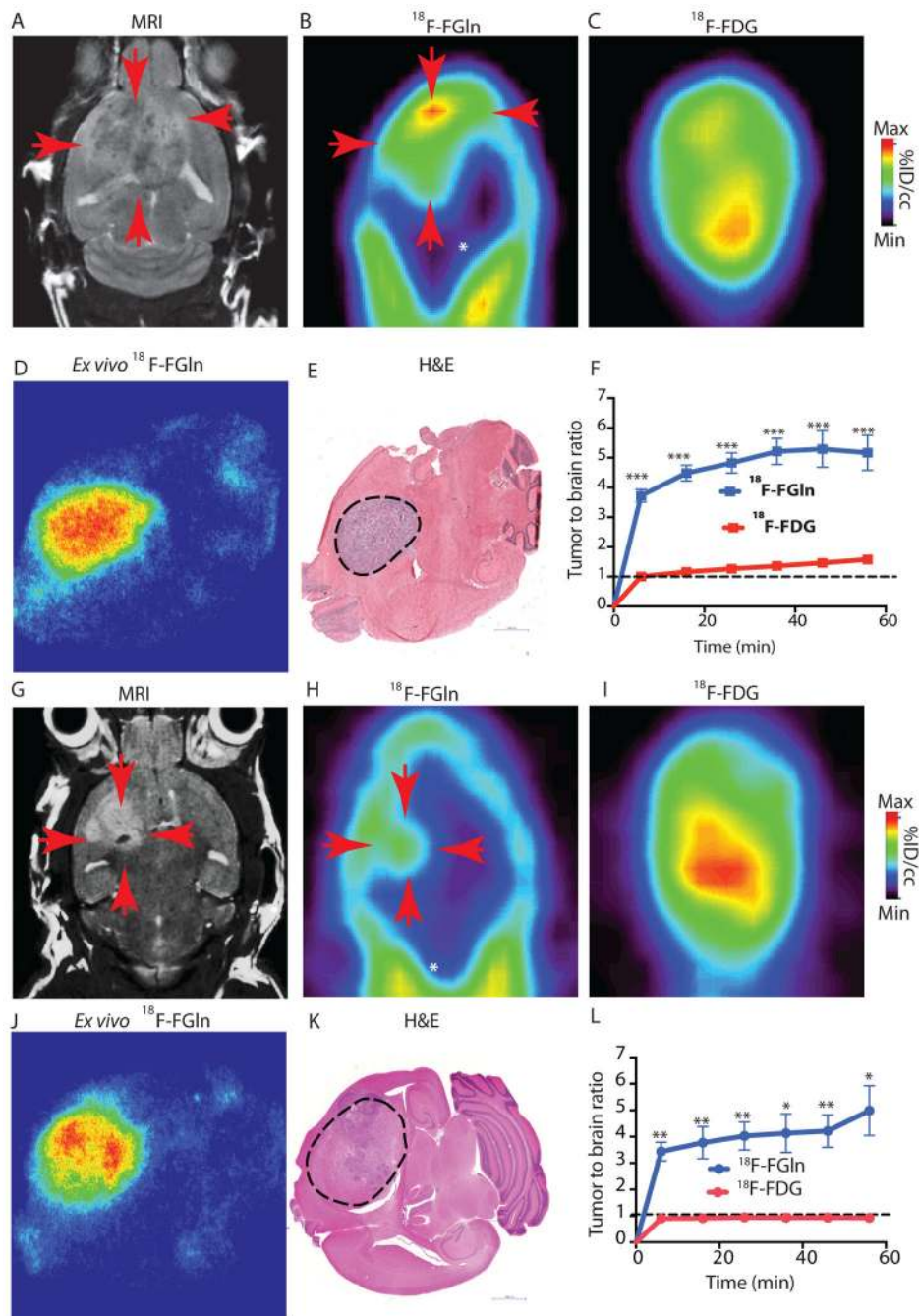
For all graphs, data are represented as the means ± s.e.m.

Fig 2. ^{18}F-FGln shows high tumor uptake compared to background in gliomas

A. Representative coronal MRI depicting tumor (red arrows) in genetically engineered RCAS-PDGF, PTEN −/− mice.

B. Coronal ^{18}F-FGln PET image illustrating high tumor uptake (red arrows) compared to surrounding non-neoplastic brain (white asterisk).

C. Coronal ^{18}F-FDG PET image from the same animal.

D. Representative ex-vivo ^{18}F-FGln autoradiogram from a RCAS-PDGF PTEN −/− animal.

E. Histological section from the same animal depicted in D, showing the tumor region (dotted black line). Scale bars represent 1000 μM.

F. Time activity curve illustrating tumor to background ratio with ^{18}F-FGln (blue) compared to ^{18}F-FDG (red) in RCAS-PDGF PTEN null animals (n=6 each). Dotted black line indicates an equal tumor to brain ratio of 1:1. Statistical significance was determined by two-sided, unpaired, Student's t-test; *** indicates p < 0.0001.

G. Representative coronal MRI showing tumor (red arrows) in mice orthotopically implanted with TS603 (IDH1 R132H) glioma cells.

H. Coronal ^{18}F-FGln PET image from the same animal illustrating high tumor uptake (red arrows) compared to surrounding non-neoplastic brain (white asterisk).

I. Coronal ^{18}F-FDG PET image from the same animal.

J. Ex-vivo ^{18}F-FGln autoradiogram from the same animal.

K. Histological section from the same animal. Scale bars represent 1000 μM.

L. Time activity curve illustrating tumor to background ratio with ^{18}F-FGln (blue, (n=4 for 36 minute imaging time point, n=3 for all other time points) compared to ^{18}F-FDG (red, n=3 for all time points) in mice orthotopically implanted with TS603 (IDH1 R132H) glioma cells. Dotted black line indicates an equal tumor to brain ratio of 1:1. Statistical significance was determined by two-sided, unpaired, Student's t-test; * indicates p< 0.05 and ** p<0.01. For all graphs, data are represented as the means ± s.e.m.
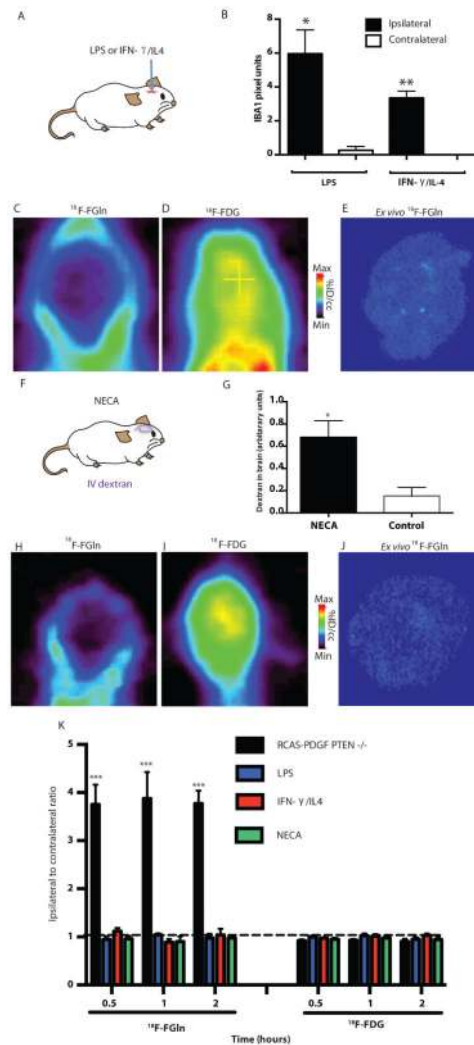
Fig 3. ^{18}F-FGln shows no uptake in animals with neuroinflammation or a disrupted BBB

A. Animal models of neuroinflammation were created by intra-cerebral injection of LPS or a combination of IFN-γ and IL4.

B. Quantification of IBA1-positive activated microglia/macrophages at the site ipsilateral to the lesion (black bars) or contralateral to the lesion (white bars) from animals injected with LPS (n=3) or IFN-γ/IL4 (n=3). Statistical significance was determined by two-sided, unpaired Student's t-test; * indicates p< 0.05 and ** p<0.01.

C. Representative coronal ^{18}F-FGln PET image from an LPS-injected animal.

D. Representative ^{18}F-FDG PET image from the same animal.

E. Representative ex-vivo ^{18}F-FGln autoradiogram from the same animal.

F. Blood brain barrier was disrupted (as measured by extracerebral IV dextran) by treating animals with NECA [1-(6-amino-9*H*-purin-9-yl)-1-deoxy-*N*-ethyl-β-D-ribofuranuronamide], a combined A1 and A2 adenosine receptor agonist that increases BBB permeability by increasing spaces between endothelial cells.

G. Measurement of extracerebral IV dextran in NECA-treated or vehicle-treated animals (n=3, each condition). Statistical significance was determined by two-sided, unpaired Student's t-test; * indicates p< 0.05

H. Representative coronal ^{18}F-FGln PET image from a NECA-injected animal.

I. Representative ^{18}F-FDG PET image from the same animal.

J. Representative ex-vivo ^{18}F-FGln autoradiogram from the same animal.

K. Comparison of ^{18}F-FGln uptake and ^{18}F-FDG uptake in RCAS-PDGF, PTEN −/− (black bars, n=6 for ^{18}F-FGln and n=5 for ^{18}F-FDG at all time points) with animals injected intra-cerebrally with LPS (blue bars, for both ^{18}F-FGln and ^{18}F-FDG n=5 at 0.5 h, n= 4 at 1 h, n=4 at 2 h) or IFN-γ/IL4 (red bars, n=6 for[18]F-FGln at all time points; for ^{18}F-FDG, n=5 at 0.5 h, and n=6 at 1 h and 2 h), or intravenously with NECA (green bars, n=5 for ^{18}F-FGln and n =4 for ^{18}F-FDG at all time points). Dotted black line indicates an equivalent lesion to brain ratio of 1:1.

Statistical significance was determined by two-sided ANOVA. For all graphs, data are represented as the means ± s.e.m. *** indicates p<0.001.
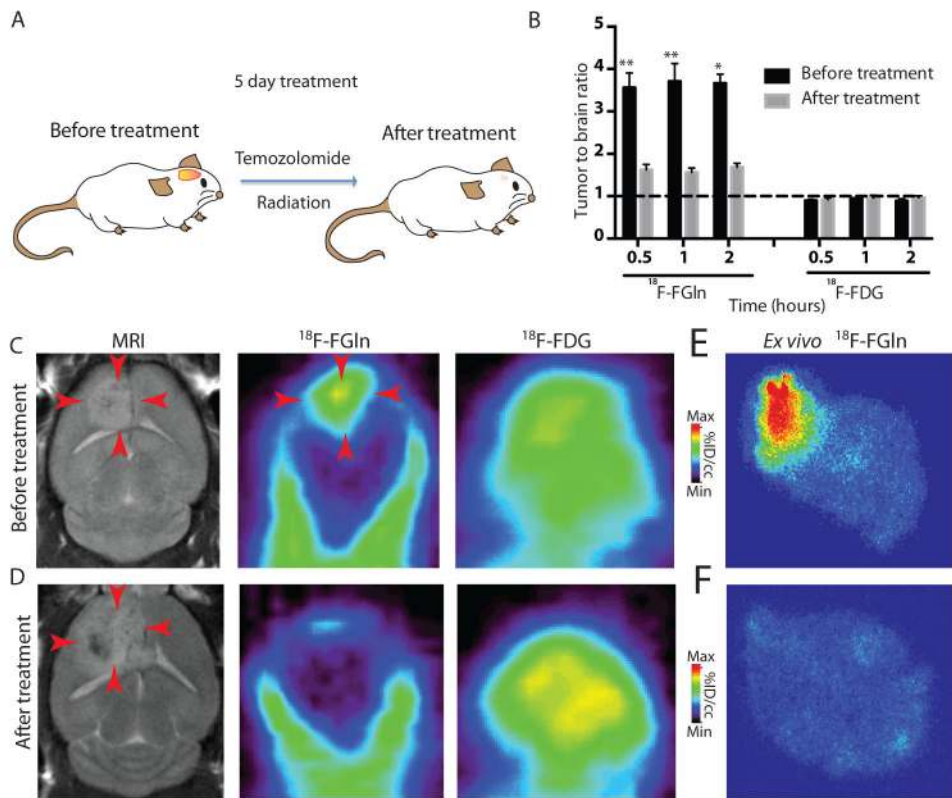
Fig 4. ^{18}F-FGln uptake in gliomas is reduced after chemo/radiation therapy

A. Treatment regimen in RCAS-PDGF, PTEN −/− mice consisted of 5 days of chemotherapy (temozolomide 50 mg/ml) and radiation therapy (155 cGy).

B. The same animal was imaged with either ^{18}F-FGln or ^{18}F-FDG before treatment (black bars, n=8 for ^{18}F-FGln and n=6 for ^{18}F-FDG for all time points) and after treatment (gray bars, n=9 for ^{18}F-FGln for 0.5 and 1 h and n=6 for 2 h time points and n=6 for ^{18}F-FDG for all time points). Dotted black line indicates an equivalent tumor to brain ratio of 1:1. For all graphs, data are represented as the means ± s.e.m. Statistical significance was determined by Wilcoxon matched-pairs signed rank *t* test (because the same animal was imaged before and after treatment), * indicates p< 0.05 and ** p<0.01.

C. Representative before-treatment images of MRI, ^{18}F-FGln PET, and ^{18}F-FDG PET (red arrows indicate identifiable lesion).

D. Representative after-treatment images of MRI (red arrows show post-treatment changes), ^{18}F-FGln PET, and ^{18}F-FDG PET.

E. Ex-vivo ^{18}F-FGln autoradiogram from a different animal before treatment.

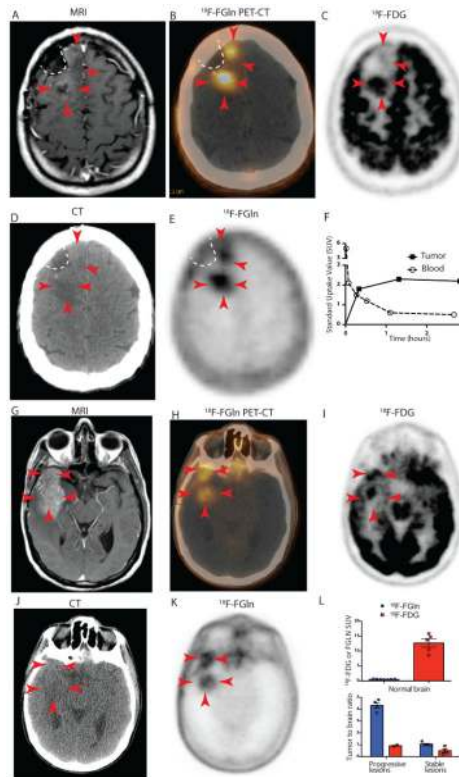**F.** Ex-vivo ^{18}F-FGln autoradiogram from a different animal after treatment.

Fig 5. ¹⁸F-FGln shows uptake in human gliomas undergoing progression

A–F. Images from patient #5

A. T1-weighted MRI with contrast enhancement from a 42-year-old IDH1-mutant oligodendroglioma patient showing tumor with minimal gadolinium enhancement (red arrows) along surgical cavity (indicated by white dotted line).

B. Fusion ¹⁸F-FGln PET-CT showing ¹⁸F-FGln uptake in areas corresponding to tumor (red arrows).

C. ¹⁸F-FDG PET image from the same patient showing high background brain avidity and tumor uptake in the posterior part of the tumor (3 red arrows), but not in the anterior portion (2 red arrows).

D. CT scan used to generate the PET-CT fusion image in B.

E. ¹⁸F-FGln PET showing high uptake in tumor with minimal uptake in the surrounding brain.

F. Time activity curve indicating standard uptake values (SUV) corresponding to tumor (black squares) and blood (clear circles).

G–K. Images from patient # 6

G. T1-weighted MRI with contrast enhancement from a 57-year-old glioblastoma patient showing tumor with gadolinium enhancement (red arrows).

H. Fusion ¹⁸F-FGln PET-CT showing ¹⁸F-FGln uptake in areas corresponding to tumor.

I. ¹⁸F-FDG PET image from same patient showing high background brain avidity and tumor uptake.

J. CT scan used to generate the PET-CT fusion image in H.

K. ^{18}F-FGln PET showing high uptake in tumor with minimal uptake in the surrounding brain.

L. Comparison of ^{18}F-FGln (blue bars) and ^{18}F-FDG (red bars) illustrates differences in background uptake with both ligands in normal brain (top panel) and tumor to brain ratios from 3 clinically stable glioma patients and 3 glioma patients with clinically progressive disease (bottom panel) (see Tables S1 and S2 for details). For all graphs, data are represented as the means ± s.e.m.